IEEE Access
Multidisciplinary | Rapid Review | Open Access Journal

Received 12 March 2023, accepted 5 April 2023, date of publication 17 April 2023, date of current version 24 April 2023.

Digital Object Identifier 10.1109/ACCESS.2023.3267736

RESEARCH ARTICLE

Research of Comprehensive Modeling of Two-Dimensional Vector Nozzle/Actuator Load/Turbofan Engine

YUAN WANG[1], WEI JIANG[2], HAIBO ZHANG[2], AND QIANGANG ZHENG[2]
[1]AECC Aero Engine Control System Institute, Wuxi 214063, China
[2]Energy and Power College, Nanjing University of Aeronautics and Astronautics, Nanjing 210016, China
Corresponding author: Yuan Wang (wangyuan139@126.com)

ABSTRACT To investigate the effect of the dynamic deflection process of a two-dimensional vector nozzle on its actuator load and engine performance, a comprehensive modeling method of two-dimensional vector nozzle/actuator load/turbofan engine is proposed. Firstly, based on the two-dimensional vector nozzle spatial motion model, combined with force and moment analysis, the mechanical model of vector nozzle actuation system is established; The load spectrum of the actuating system under different working conditions and deflection angles is obtained by CFD numerical simulation results; Using AMESim, the hydraulic actuation system model of two-dimensional vector nozzle is established. Finally, a two-dimensional vector nozzle/actuator/turbofan engine comprehensive model is established based on the component-level model of turbofan engine. The comprehensive model can accurately calculate the changes of main performance parameters such as engine rotor speed, thrust and pre-turbine temperature when the nozzle vector deflects. The simulation results show that the load on the nozzle actuator is positively correlated with the deflection angle, and the load change will lead to the fluctuation of the output displacement of the hydraulic actuation system. During vector deflection, due to the change of engine circulation capacity and thrust coefficient, the performance parameters such as engine low-pressure rotor speed and surge margin fluctuate greatly.

INDEX TERMS 2DCD, actuator load, aircraft engine mode, comprehensive model.

I. INTRODUCTION

With the development and application of thrust vector technology, the flight performance, take-off and landing performance, maneuverability and post-stall maneuverability of aircraft have been greatly improved, so advanced aviation countries in the world give priority to it as an important technology [1]. Vector nozzle technology is the foundation and core of thrust vector technology. Among various vector nozzle schemes, 2D vector nozzle (2DCD) has the characteristics of low infrared radiation and easy integration design with rear fuselage [2], so 2D vector nozzle is an essential technology for future advanced fighters [3].

Since the 1970s, NASA, military, aircraft and engine companies in the United States have carried out a series of two-dimensional vector nozzle research plans and wind tunnel test plans for thrust vector aircraft [4]. In the 1980s, the United States carried out a full-scale, non-flying-weight two-dimensional nozzle design and ground tests, and on this basis, carried out ground and flight verification tests of flying-weight nozzles [5]. Since 1989, the two-dimensional vector nozzle has been tested on the F-15. In the 1990s, thrust vector aircraft made great progress in engineering, and a new type of vector thrust aircraft was studied [6]. After long-term theoretical and experimental research of thrust vector technology and the accumulation of several demonstration test projects, at the beginning of the 21st century, the thrust vector technology was successfully applied to the main fighters and stealth aircraft of the Air Force. In the academic field, scholars at home and abroad have done a lot of work in numerical simulation and experiments on the internal flow characteristics of two-dimensional vector nozzle [7], [8], [9],

The associate editor coordinating the review of this manuscript and approving it for publication was Rosario Pecora.

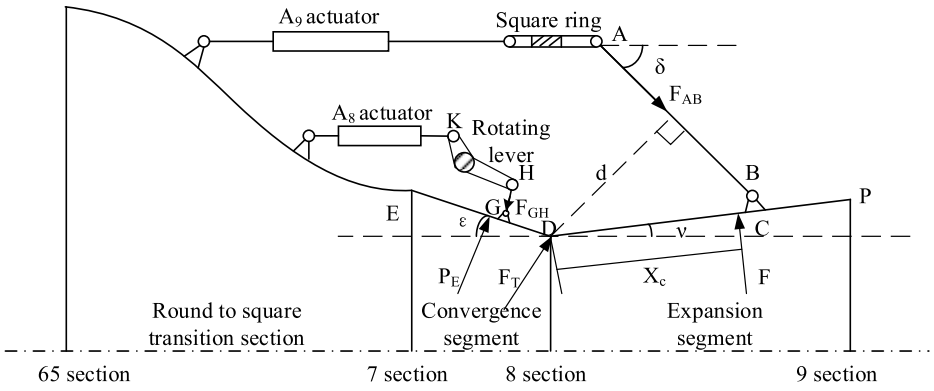

FIGURE 1. Schematic diagram of spatial motion and force of two-dimensional vector nozzle.

[10], [11], [12], [13], [14], [15], [16]. However, the research on actuator load and vector nozzle/engine integrated model is mostly focused on axisymmetric vector nozzle. Zhang [17] put forward a coupling modeling method of axisymmetric vector nozzle spatial kinematics model and vector deflection CFD model, which solved the problem that the load of A9 actuator is unknown when axisymmetric vector nozzle actually works. Huang [18] systematically modeled the vector nozzle control device based on AMESim, and studied the steady-state performance, dynamic performance, robustness and performance when the fault returns. As a necessary component of the engine, the working state of the engine fluctuates violently when the vector is deflected, so Cai [19] have established a dynamic model of turbofan engine with axisymmetric vector nozzle, and the linear active disturbance rejection control is adopted to reduce the variation amplitude of engine state parameters under the traditional PID closed-loop control. Qu studied the influence of vector deflection on the working state of the engine under open-loop control; Li [21] established a micro turbojet vector propulsion system model based on experimental data and mechanism model. Li's model based on experimental data is difficult to ensure the accuracy requirements, Cai and Qu only established the mathematical model of the engine with axisymmetric vector nozzle. However, the structure and kinematics model of two-dimensional vector nozzle are quite different from that of axisymmetric vector nozzle. It is impossible to obtain the influence of the vector deflection of the two-dimensional vector nozzle on the working state of the engine. Therefore, it is of great significance to establish a comprehensive model of two-dimensional vector nozzle/actuator load/turbofan engine based on mechanism for the stability and accurate control of engine and nozzle in the next step.

In this paper, the aerodynamic characteristics of the two-dimensional vector nozzle are combined with the mechanical motion mechanism of the nozzle. Based on CFD numerical simulation, the aerodynamic performance model of the vector nozzle is established, and the actuator model which can reflect the change of the vector deflection aerodynamic load is established. The comprehensive model of the two-dimensional vector nozzle/actuator load/turbofan engine which can reflect the influence of the change of the vector deflection aerodynamic load on the throat area control system is established by Simulink/AMESim.

II. MECHANICAL MODEL

The structural diagram of the two-dimensional vector nozzle is shown in Figure 1, and its convergent section and divergent section can be continuously adjusted. The upper expansion adjusting plate and the lower expansion adjusting plate are respectively driven by an A9 actuator, the front end of the A9 actuator is hinged with the casing, and the rear end is hinged with the square ring connecting rod mechanism. The three-dimensional structural diagram of the square ring linkage mechanism is shown in Figure 2, and the square ring can only move horizontally in the groove on the side wall of the casing, thus ensuring that the A9 actuator always maintains a horizontal position. The rear end of the square ring linkage mechanism is hinged with the expansion adjusting plate. When the output displacement of the A9 actuator changes, the square ring moves horizontally, thus driving the pull rod and the expansion adjusting plate to move. When the upper and lower A9 actuators synchronously output displacement, adjust the A9 cross-sectional area; When the output displacements of the upper and lower A9 actuators are different, the section of A9 tilts to realize pitching thrust.

The A8 actuating system of two-dimensional nozzle is connected with A8 actuating cylinder and convergence adjusting plate by rocker arm, and its structure diagram is shown in Figure 3. The front end of the rocker arm is hinged with the A8 actuating cylinder, and the rear end is hinged with the convergence adjusting piece through the pull rod. When the A8 actuator outputs displacement, the rocker arm rotates around its rotating rod, thus driving the pull rod and the convergence adjusting plate to rotate, thus realizing the change of A8 throat area.

The force acting on the actuating system of two-dimensional vector nozzle is shown in Figure 1, and the side

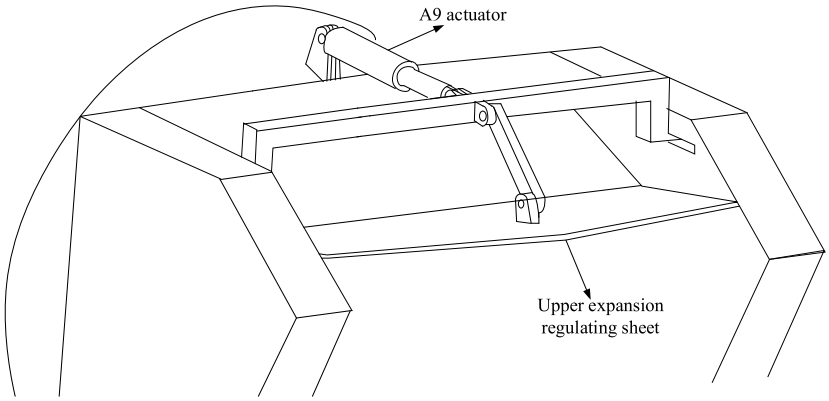

FIGURE 2. Structural sketch of expansion adjusting plate.

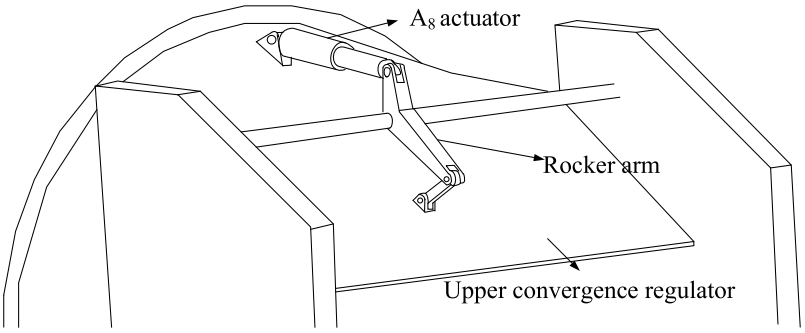

FIGURE 3. Structure diagram of convergence adjusting piece.

plate of the two-dimensional nozzle is fixed and cannot be adjusted. When analyzing the force acting on the actuating system, the friction between the upper and lower adjustable plates and the side plates will not be considered for the time being. The force acting on the expansion plate includes the aerodynamic resultant force F of the expansion plate, the force F_{AB} exerted on it by the pull rod AB and the force F_{T} exerted on it by the convergence plate.

When the braking system is in a steady state, it can be obtained from the moment balance between the convergent adjusting plate and the divergent adjusting plate at point D:

$$F_{AB} \times d = F \times X_C \tag{1}$$

d is the distance from the pull rod AB to the point D, and X_{C} is the position of the aerodynamic resultant force in the expansion section.

d can be calculated by equation (2):

$$d = \sin(\upsilon + \delta) \cdot \left[\frac{L_h}{\tan(\upsilon + \delta)} + L_{DC} \right] \tag{2}$$

υ is the expansion angle of the expansion adjusting plate, δ is the included angle between the pull rod AB and the horizontal axis, and L_h is the distance from point B to point C.

δ calculation equation is:

$$\delta = \arcsin\left(\frac{R_A - R_D - L_{DC} \cdot \sin\upsilon - L_h \cdot \cos\upsilon}{L_{AB}} \right) \tag{3}$$

R_A is the distance from point A to the nozzle axis, R_D is half the throat height, L_{DB} is the distance from point D to point B, and L_{AB} is the length of pull rod AB.

The force component of the pull rod AB along the horizontal direction is balanced by the A9 actuator, and then the output force of the A9 actuator can be solved as follows:

$$F_{A_9} = F_{AB} \cdot \cos\delta \tag{4}$$

The acting force F_T of the expansion adjusting plate on the convergence adjusting plate is obtained by Equation (5):

$$F_T = -(F + F_{AB}) \tag{5}$$

To simplify the calculation, decompose it along the X and Y axes, and we can get:

$$\begin{aligned} F_{T_X} &= -(-F \cdot \sin\nu + F_{AB} \cdot \cos\delta) \\ F_{T_Y} &= -(F \cdot \cos\nu - F_{AB} \cdot \sin\delta) \end{aligned} \tag{6}$$

The force exerted by the pull rod GH on the convergence adjusting plate can be obtained from the moment balance of the connection point E between the convergence adjusting

plate and the casing:

$$F_{GH} = \frac{F_{T_X} \cdot L_{ED} \cdot \sin\varepsilon + F_{T_Y} \cdot L_{ED} \cdot \cos\varepsilon + P_E \cdot X_E}{d_1} \quad (7)$$

d_1 is the distance from the point E to the GH point, L_{ED} is the length of the convergence adjusting plate, ε is the convergence angle of the convergence adjusting plate, and P_E and X_E are the aerodynamic resultant force and center of the convergence adjusting plate.

The output force of A8 actuator can be further solved by the force acting on the pull rod GH.

When the actuating system is in a stable state, the moment balance between A8 actuating cylinder and connecting rod GH about fixed point N can be obtained as follows:

$$F_{A8} \times d_2 = F_{GH} \times d_3 \quad (8)$$

F_{A8} is the output force of actuator A8, d_2 is the distance from actuator MK to fixed point N, and d_3 is the distance from rod GH to fixed point N.

d_2 can be expressed by Equation (9):

$$d_2 = L_{KN} \cdot \sin\theta \quad (9)$$

where L_{KN} is the length of the left KN of the rocker arm, and θ is the included angle between the actuator MK and the left KN of the rocker arm.

θ can be represented by equation (10):

$$\theta = \arccos\left(\frac{L_{MK}^2 + L_{NK}^2 - L_{MN}^2}{2 \cdot L_{MK} \cdot L_{NK}}\right) \quad (10)$$

where L_{MN} is the distance between point m and fixed point n of rocker arm.

The distance of the dotted line NG can be expressed by Equation (11):

$$L_{NG} = \sqrt{L_{EG}^2 + L_{EN}^2 - 2 \cdot L_{EG} \cdot L_{EN} \cdot \cos(\varepsilon + \zeta)} \quad (11)$$

where L_{EG} is the distance between point E and hinge point G, L_{EN} is the distance between point E and fixed point N, and ζ is the included angle between connecting line EN and the central axis.

The included angle γ between the right end NH of the rocker arm and the rod GH can be expressed by Equation (12):

$$\gamma = \arccos\left(\frac{L_{NH}^2 + L_{GH}^2 - L_{NG}^2}{2 \cdot L_{NH} \cdot L_{GH}}\right) \quad (12)$$

where L_{NG} is the length of the rod NG and L_{HG} is the length of the right half of the rocker arm.

Then the distance d_3 from the rod GH to the fixed point n can be expressed by equation (13).

$$d_3 = L_{HG} \cdot \sin\gamma \quad (13)$$

The expression of the output force F_{A8} of A8 actuator can be obtained by bringing equations (9) to (13) into equation (8).

The included angle β between the rod HG and the dotted line NG can be expressed by Equation (14):

$$\beta = \arccos\left(\frac{L_{HG}^2 + L_{NG}^2 - L_{NH}^2}{2 \cdot L_{HG} \cdot L_{NG}}\right) \quad (14)$$

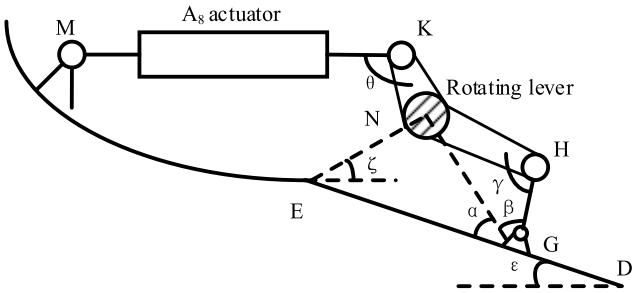

FIGURE 4. Enlarged view of convergent section structure.

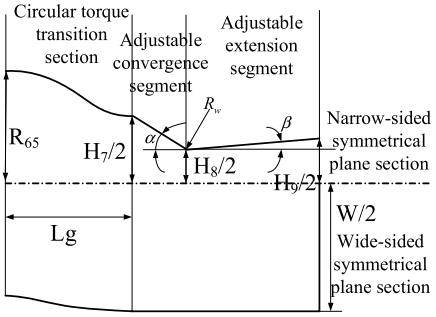

FIGURE 5. 2DCD 2D schematic diagram.

The included angle α between rod EG and dotted line NG can be expressed by equation (15):

$$\alpha = arc\sin\left(\frac{L_{EN}}{L_{GN}} \cdot \sin(\varepsilon + \zeta)\right) \quad (15)$$

Then the distance d1 from the HG point to the E point of the pole can be expressed by equation (16):

$$d_1 = L_{EG} \cdot \sin(\alpha + \beta) \quad (16)$$

By introducing the equation (7), the force exerted by the pull rod GH on the convergence regulator can be obtained.

III. ACTUATOR LOAD MODEL

The two-dimensional vector nozzle consists of a circular torque transition section and a main nozzle section (adjustable convergence section and adjustable expansion section), and its simplified model is shown in Figure 5. The circular torque transition section is not adjustable, which realizes the transition from the circular outlet of afterburner to the rectangular inlet of the main nozzle section. The main nozzle section consists of two parallel side plates, left and right, and two adjustable adjusting plates, upper and lower. Both convergent section and divergent section can be adjusted to realize the change of throat area and outlet area of two-dimensional vector nozzle, so as to meet the requirements of aircraft under different working conditions and provide vector thrust and reverse thrust. H_7, H_8 and H_9 are the heights of the inlet, throat and outlet of the main nozzle respectively; W is the width between the two side walls; α is the convergent half angle; β is the expansion half angle; R_w is the radius of throat

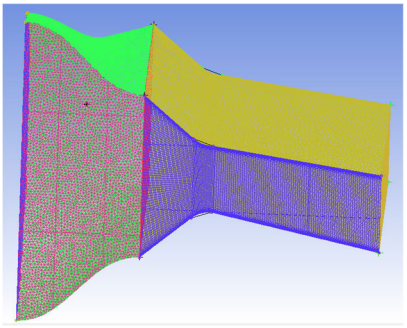

FIGURE 6. Grid division.

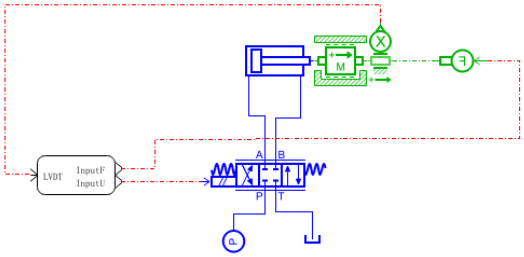

FIGURE 7. A8 actuation system model.

arc; L_g represents the length of the circular torque transition section [22].

The grid model of two-dimensional vector nozzle is shown in Figure 6. In order to reduce the difficulty of grid division and ensure the accuracy of calculation, unstructured grid is used in the transition section of circular torque, structured grid is used in the convergence and expansion section, and encryption is carried out near the nozzle wall.

CFD numerical simulation of vector deflection of two-dimensional vector nozzle is based on Fluent software, and S-A single equation model is selected as turbulence model [23]. The nozzle inlet is given the pressure inlet boundary condition, and the nozzle outlet is given the pressure outlet inlet. The specific values are determined by the engine model.

The nozzle thrust calculation equation is as follows:

$$\begin{cases} F_x = \sum \Delta m \cdot u + (p - p_a)\,\Delta A_x \\ F_y = \sum \Delta m \cdot v + (p - p_a)\,\Delta A_y \\ F_z = \sum \Delta m \cdot w + (p - p_a)\,\Delta A_z \end{cases} \tag{17}$$

where F_x, F_y and F_z respectively represent axial thrust, yaw thrust and pitch thrust; Δm is the mass flow of each micro-element area of the outlet section A9.

The effective vector angle β_0 is:

$$\beta_0 = \arctan(F_z/F_x) \tag{18}$$

The total thrust F is:

$$F = \sqrt{F_x^2 + F_y^2 + F_z^2} \tag{19}$$

The thrust coefficient C_{th} is the ratio of the actual total thrust to the ideal total thrust at the nozzle outlet section, namely:

$$C_{th} = F/F_i \tag{20}$$

The aerodynamic resultant force of the expansion tab is:

$$F = \int_0^{L_{DP}} P(x) \cdot S(x) dx \tag{21}$$

where $P(x)$ is the static pressure distribution along the axial center line of the expansion tab, and the fitting curve of the static pressure distribution at the center line of the upper and lower expansion tabs of the two-dimensional nozzle in each deflection state obtained by Fluent calculation is solved, where $S(x)$ is the distribution along the axial area of the expansion tab and the integral interval is the length of the expansion section.

The position of the action point of aerodynamic resultant force in the expansion section is:

$$X_C = \frac{1}{F} \int_0^{L_{DP}} P(x) \cdot S(x) \cdot x dx \tag{22}$$

The aerodynamic force of that convergence regulator are as follows:

$$P_E = \int_0^{L_{ED}} P_e(x) \cdot S(x) dx \tag{23}$$

In the equation, the upper integral limit L_{ED} is the length of the convergence regulator, and $P_e(x)$ is the aerodynamic load distribution along the convergence regulator. Similarly, it can be calculated and solved by vector deflection Fluent.

IV. COMPREHENSIVE MODEL

Hydraulic servo control system is a feedback control system with hydraulic power components as driving devices [24], [25]. In this system, the output (displacement, speed, force, etc.) can automatically, quickly and accurately reproduce the changing law of the input, and it is also a power amplifier [26], [27]. In this section, based on the load characteristics, the simplified model of A8 actuating system including electromagnetic directional valve, hydraulic actuator, displacement sensor, external load force model and PID controller is established by using AMESim software.

Set the input parameters of A8 actuating system as displacement command and external load force, and the output parameters as displacement feedback from displacement sensor. The established AMESim model is shown in Figure 7. Set the input parameters of A8 actuating system as displacement command and external load force, and the output parameters as displacement feedback from displacement sensor. The established AMESim model is shown in Figure 7.

The engine component-level model in this paper is a twin-shaft mixed-row turbofan engine with small bypass ratio. Figure 8 shows the overall structure of the engine, and its main components include supersonic inlet, fan, compressor, external bypass, combustion chamber, high-pressure turbine, low-pressure turbine, mixing chamber, afterburner and tail nozzle. 2∼22 sections are fans, 13∼16 sections are external ducts, 25∼3 sections are compressors, 3∼41 sections are

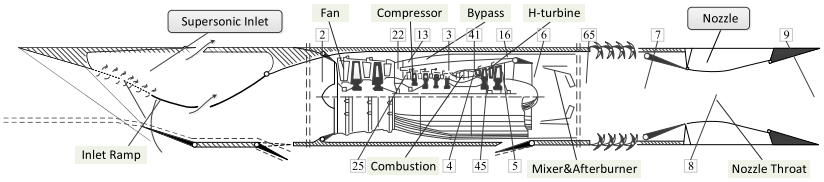

FIGURE 8. Schematic diagram of turbofan engine structure.

combustion chambers, 41∼45 sections are high-pressure turbines, 45∼5 sections are low-pressure turbines, 6∼7 sections are mixing chambers and afterburner, 7∼9 sections are tail nozzles, and 8 sections are nozzle throat areas.

The component-level model of aero-engine dynamic process includes component model and solution of common working equation. The component model simulates the aerodynamic and thermodynamic process in the component, which is not described in detail in this paper. The matching relationship between components in the steady-state process is determined by the relationship of continuous flow, power balance and pressure balance. In this paper, the relative physical speed N_L of the low-pressure rotor, the relative physical speed N_H of the high-pressure rotor, the fan pressure ratio coefficient Z_f, the high-pressure compressor pressure ratio coefficient Z_{cH}, the high-pressure turbine pressure ratio coefficient Z_{tH} and the low-pressure turbine pressure ratio coefficient Z_{tL} are selected as unknown parameters to solve the component-level model, and six unknown parameters correspond to six independent equations, as shown in Equation (24).

$$\varepsilon_i(U) = f_i(N) = 0 (i = 1 \sim 6) \tag{24}$$

where N represents a vector consisting of six initial guesses, which can be expressed as

$$\begin{aligned} N &= [n_1, n_2, n_3, n_4, n_5, n_6]^T \\ &= \left[N_L, N_H, Z_f, Z_{cH}, Z_{tL}, Zn_{tH}\right]^T \end{aligned} \tag{25}$$

The six equilibrium equations are as follows:

(1) The residual equation of the balance between the fan consumption power W_f and the power W_{tL} provided by the low-pressure turbine is obtained from the power balance of the low-pressure rotor:

$$\varepsilon_1 = \frac{W_{tL}\eta_{tL} - W_f}{W_{tL}\eta_{tL}} \tag{26}$$

where η_{tL} is the efficiency of the low-pressure rotor.

(2) Based on the power balance of the high-pressure rotor, the residual equation of the balance between the power consumption W_{cH} of the high-pressure compressor and the power output W_{ext} of the high-pressure shaft and the power W_{tH} provided by the high-pressure turbine is obtained:

$$\varepsilon_2 = \frac{W_{tH}\eta_{tH} - (W_{cH} + W_{ext})}{W_{tH}\eta_{tH}} \tag{27}$$

where η_{tH} is the efficiency of the low-pressure rotor.

(3) Based on the flow balance of high-pressure turbine, the actual inlet flow $m_{41,c}$ of high-pressure turbine is obtained and the residual equation of turbine flow $m_{41,cx}$ is obtained by three-dimensional interpolation with the characteristics of high-pressure turbine:

$$\varepsilon_3 = \frac{m_{41,c} - m_{41,cx}}{m_{41,c}} \tag{28}$$

(4) Based on the low-pressure turbine flow balance, the actual low-pressure turbine inlet flow $m_{45,c}$ and the low-pressure turbine characteristics are interpolated to obtain the residual equation of turbine flow $m_{45,cx}$:

$$\varepsilon_4 = \frac{m_{45,c} - m_{45,cx}}{m_{45,c}} \tag{29}$$

(5) Based on the static pressure balance at the outlet of the external culvert, the residual equation between the internal static pressure P_6 of the engine and the static pressure P_{16} of the external culvert is obtained:

$$\varepsilon_5 = \frac{P_6 - P_{16}}{P_6} \tag{30}$$

(6) The residual equation of the nozzle throat static pressure P_8 and the static pressures $P_{8,c}$ calculated according to the internal flow characteristics of the nozzle is obtained from the nozzle throat static pressure balance:

$$\varepsilon_6 = \frac{P_8 - P_{8,c}}{P_8} \tag{31}$$

In the dynamic process of the engine, the rotor power of the high and low pressure turbine is no longer balanced with the rotor power of the compression part, so the deviation value will change the rotor speed, and the balance equation is replaced by the dynamic equation of the high and low pressure rotor.

$$\begin{cases} \frac{dN_L}{dt} = (W_{tL}\eta_{tL} - W_f) \Big/ \left[N_L J_L \left(\frac{\pi}{30}\right)^2\right] \\ \frac{dN_H}{dt} = (W_{tH}\eta_{tH} - W_{cH} - W_{ext}) \Big/ \left[N_H J_H \left(\frac{\pi}{30}\right)^2\right] \end{cases} \tag{32}$$

where J_L and J_H are the moment of inertia of the low pressure shaft and the moment of inertia of the high pressure shaft respectively, and their values are obtained with reference to Gasturb software. In the dynamic process, the current rotational speed (N_2) is obtained by superposition of the previous rotational speed (N_1) by Euler method, namely:

$$\begin{cases} N_{L2} = N_{L1} + dN_L \Delta t \\ N_{H2} = N_{H1} + dN_H \Delta t \end{cases} \tag{33}$$

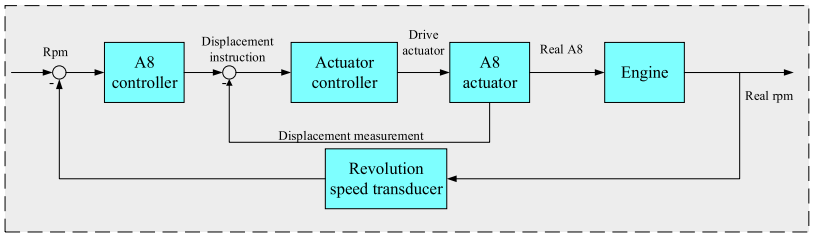

FIGURE 9. Structure block diagram of vector deflection comprehensive model.

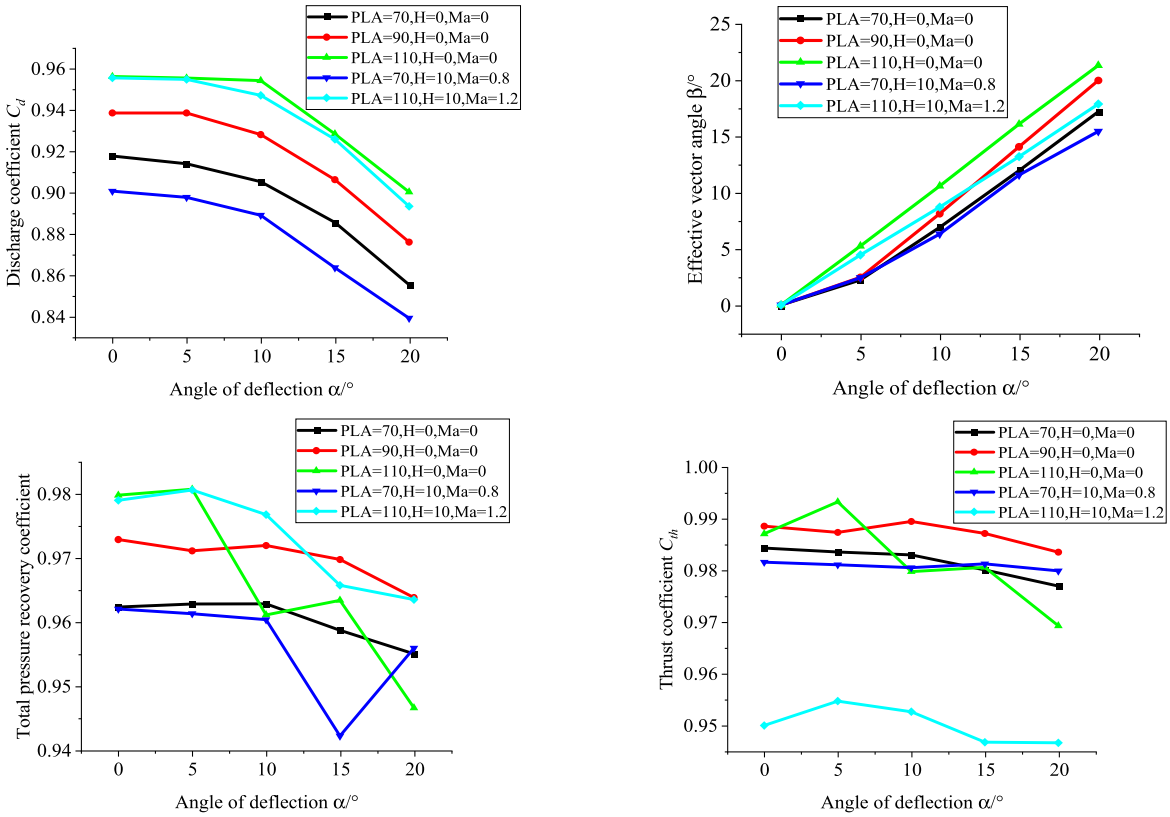

FIGURE 10. Structure block diagram of vector deflection comprehensive model.

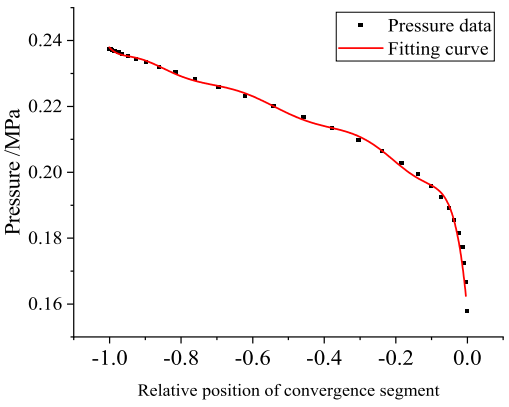

FIGURE 11. Pressure distribution in convergent section.

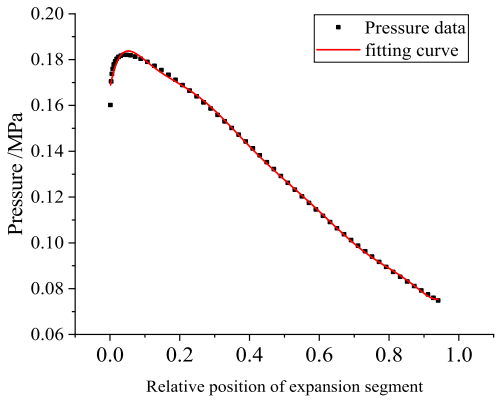

FIGURE 12. Pressure distribution in expansion section.

In order to obtain the aerodynamic thermodynamic parameters and performance parameters of each section of the engine, the Newton-Raphson method with fast convergence speed and small amount of calculation is used to iteratively calculate the balance equation.

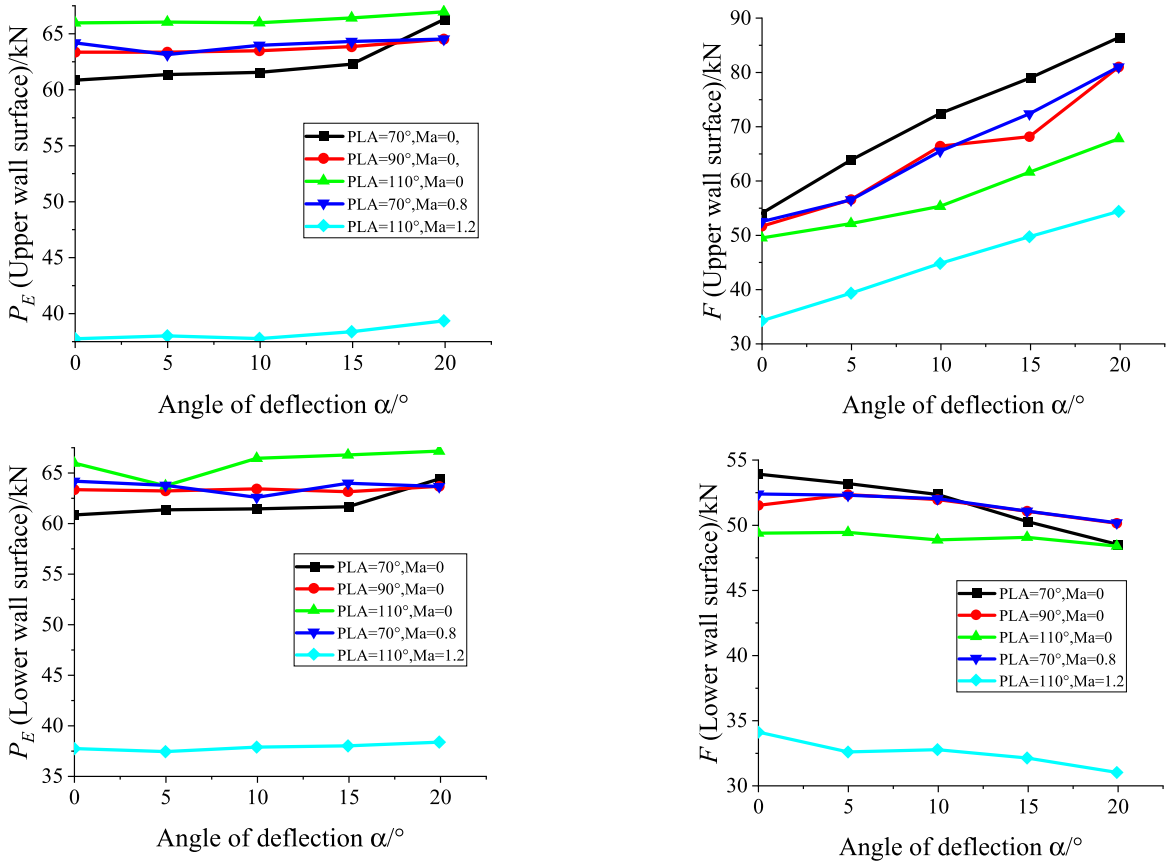

FIGURE 13. Load condition of the adjusting plate of the two-dimensional vector nozzle.

The effect of vector deflection on engine performance is mainly reflected in the change of effective throat area and nozzle thrust coefficient. The vector deviation transfer causes the nozzle throat to tilt, resulting in the reduction of the effective throat area, thus affecting the engine working state, while the change of thrust coefficient causes the change of the engine output thrust. Therefore, the effective throat area coefficient C_{A8e} is defined as:

$$C_{A_{8e}} = \frac{\dot{m}_a}{\dot{m}_{Axis}} \tag{34}$$

where $\dot{m}_{Axis}$ is the nozzle flow calculated by CFD in the undeflected state and $\dot{m}_a$ is the nozzle flow calculated by CFD in the deflected state.

Therefore, the calculation equation of P_{8c} in the static pressure balance equation of the nozzle throat is as follows:

$$P_{8c} = \frac{m_{g8} \cdot \sqrt{T_8} \cdot q\left(\lambda_8\right)}{\sqrt{\frac{k_8}{R_8} \cdot \left(\frac{2}{k_8+1}\right)^{\frac{k_8+1}{k_8-1}}} \cdot A_8 \cdot C_{A_{8e}}} \tag{35}$$

Define relative thrust coefficient C_{thR}:

$$C_{thR} = C_{th}/C_{thAxis} \tag{36}$$

where C_{th} is that thrust coefficient of the deflect nozzle under different work conditions, and C_{thAxis} is the reference thrust coefficient of the undeflected nozzle.

When the vector deflects, the equation for calculating the resultant thrust of the engine vector is:

$$F = (\dot{m}_{a8} \cdot v_9 - \dot{m}_{a2} \cdot v_0 + (P_{S9} - P_0) \cdot A_8) \cdot C_{thR} \tag{37}$$

When the vector deflects, the effective throat area coefficient C_{A8e} changes, which changes the common working equation, while the relative thrust coefficient C_{thR} changes, which leads to the decrease of the thrust of the tail nozzle, and both of them work together to affect the change of the engine performance. The control plan of controlling the high-pressure rotor speed with the main fuel and the low-pressure rotor speed with the nozzle throat area A8 is adopted, and the vector nozzle actuator model is combined to establish a two-dimensional vector nozzle/engine comprehensive model as shown in the structural block diagram of Figure 9. The A8 actuator system is driven by two A8 actuators, and the spatial arrangement and spatial motion mode of the two actuators are introduced in detail in the mechanical model in Section II. The A8 area command calculated by A8 controller is input into the spatial kinematics model of two-dimensional vector nozzle, and the displacement command of two A8 actuators required to drive

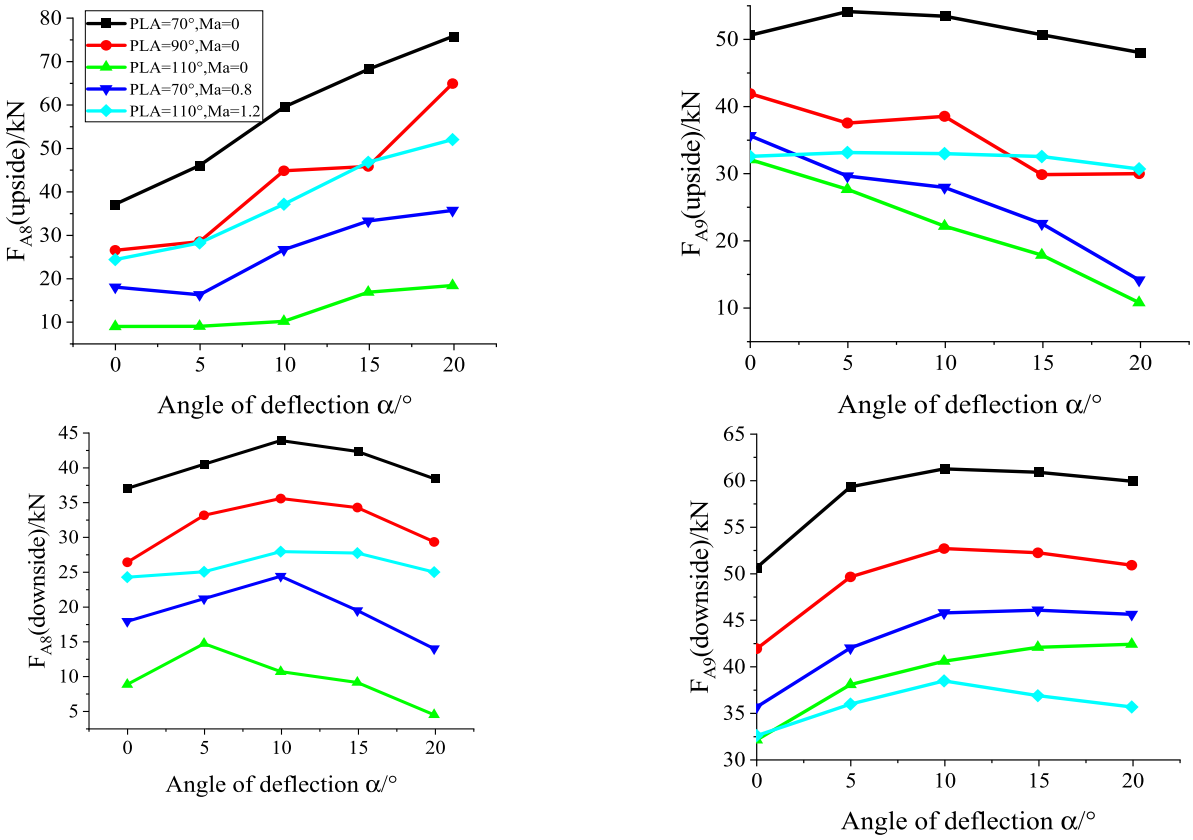

FIGURE 14. Loading conditions of actuators A8 and A9 in different states and vector deflection angles.

vector deflection is solved for actuation, thus realizing the change of real A8 cross-sectional area.

V. SIMULATION AND ANALYSIS OF VECTOR DEFLECTION

A. AERODYNAMIC PERFORMANCE SIMULATION OF TWO-DIMENSIONAL VECTOR NOZZLE

The simulation results of aerodynamic performance of two-dimensional vector nozzle under different working conditions and different vector deflection angles are shown in Figure.

As can be seen from Figure 10, with the increase of the vector deflection angle, the engine flow coefficient decreases. When the deflection angle is less than 10°, the vector deflection has little influence on the nozzle flow performance. When the deflection angle is greater than 10°, the nozzle flow performance decreases to a certain extent, and the changing trend is basically the same in different flight States. When the vector deflection angle is 20°, the nozzle flow capacity decreases by about 6.5%, and the engine state is greater at the same deflection angle. the effective vector angle of the engine is slightly smaller than the vector deflection angle, which is especially obvious in the high-altitude flight state. Similarly, the greater the engine state, the closer the effective vector angle is to the vector deflection angle, and the better the linearity between them.

With the increase of the vector deflection angle, the total pressure recovery coefficient of the engine decreases. When the deflection angle is less than 5°, the vector deflection has little influence on the total pressure loss of the nozzle, and when the deflection angle is greater than 5°, the total pressure loss decreases to a certain extent, and the change trend is basically the same in different flight states. Vector deflection has little effect on thrust coefficient. Under different flight conditions and different engine conditions, with the increase of vector deflection angle, thrust coefficient shows a slight downward trend. When the vector deflection angle is 20°, the relative thrust coefficient of the nozzle decreases by about 0.5%.

B. SIMULATION OF LOAD CHARACTERISTICS OF ACTUATOR

According to the principle of hydrodynamics, the pressure on the wall in the flowing pipeline is equal to the pressure at the point where the velocity is 0. Therefore, it is necessary to create a central surface in the process of extracting the wall pressure, extract the point on the central surface with the velocity of 0 for wall pressure function fitting, and import the upper and lower wall data in supersonic cruise state into the fitting software. The fitting result of the upper wall pressure is shown in Figure 11 and 12.

In order to calculate the load characteristics of the actuating system under different working conditions and deflection angles, this paper selects the ground point PLA=70°,

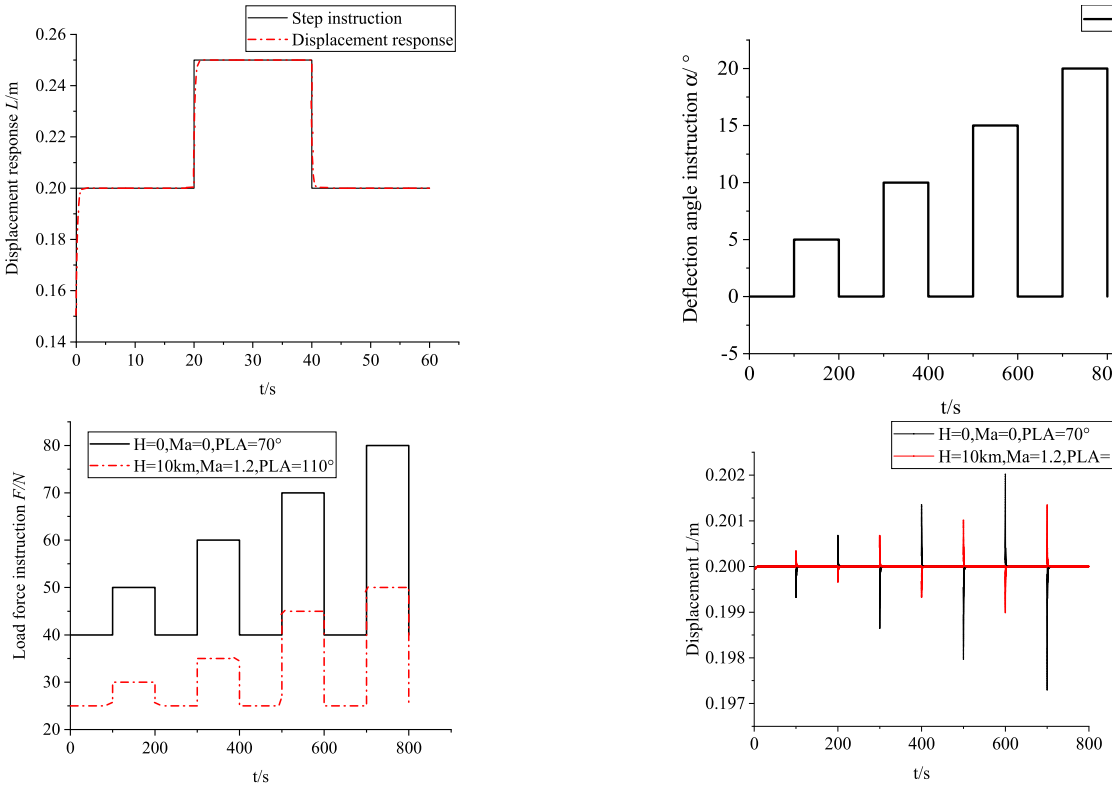

FIGURE 15. Simulation of vector deflection of actuating system.

90°, 110°, the high altitude point H=10km, Ma=0.8, PLA=70° subsonic cruise state, and the supersonic cruise state H=10km, Ma=1.2, PLA=110°. The vector deflection angles are 0°, 5°, 10°, 15° and 20° respectively. Figures 12 show the nozzle convergence and the loading conditions of the expansion section regulator under different working conditions, Figure 13 shows the loading conditions of A8 and A9 actuators.

In the process of vector deflection, the resultant force on the upper and lower clamping plates in the convergence section is basically unchanged. This is because the air flow accelerates the expansion in the binary vector nozzle and reaches the sound velocity at the throat. The impact of the vector deflection in the expansion section will not spread forward. The resultant force on the upper adjusting plate increases continuously, while the resultant force on the lower adjusting plate decreases slightly.

With the increase of the vector deflection angle, the load force of the upper A8 actuator increases continuously, and the load force of the lower A8 actuator first increases and then decreases. The load force of the upper A9 actuator decreases and the load force of the lower A9 actuator increases.

C. HYDRAULIC ACTUATOR SIMULATION

According to the calculation results of load force of A8 actuator in the state of vector deflection in the previous section, the vector deflection simulation of A8 actuator system is studied.

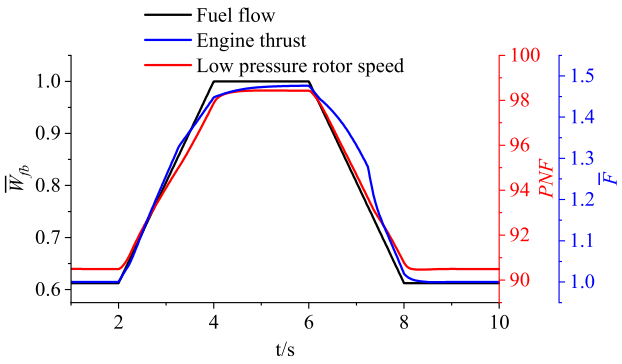

FIGURE 16. Open loop simulation.

First, input the command of centering after two 5cm steps as shown in Figure 15 and the command of constant A8 actuator load 50kN as shown in Figure 14, and the displacement response result of the actuator is shown in Figure 14.

From fig. 15, it can be concluded that the small closed-loop control loop of the hydraulic actuation system of the binary vector nozzle actuator established by AMESim software based on the load analysis results has fast response and no overshoot. According to the response results, with the increase of the vector deflection angle, the load force of the A8 actuator changes to some extent, which will lead to certain displacement fluctuation of the A8 actuator under the control of the constant displacement command. The larger

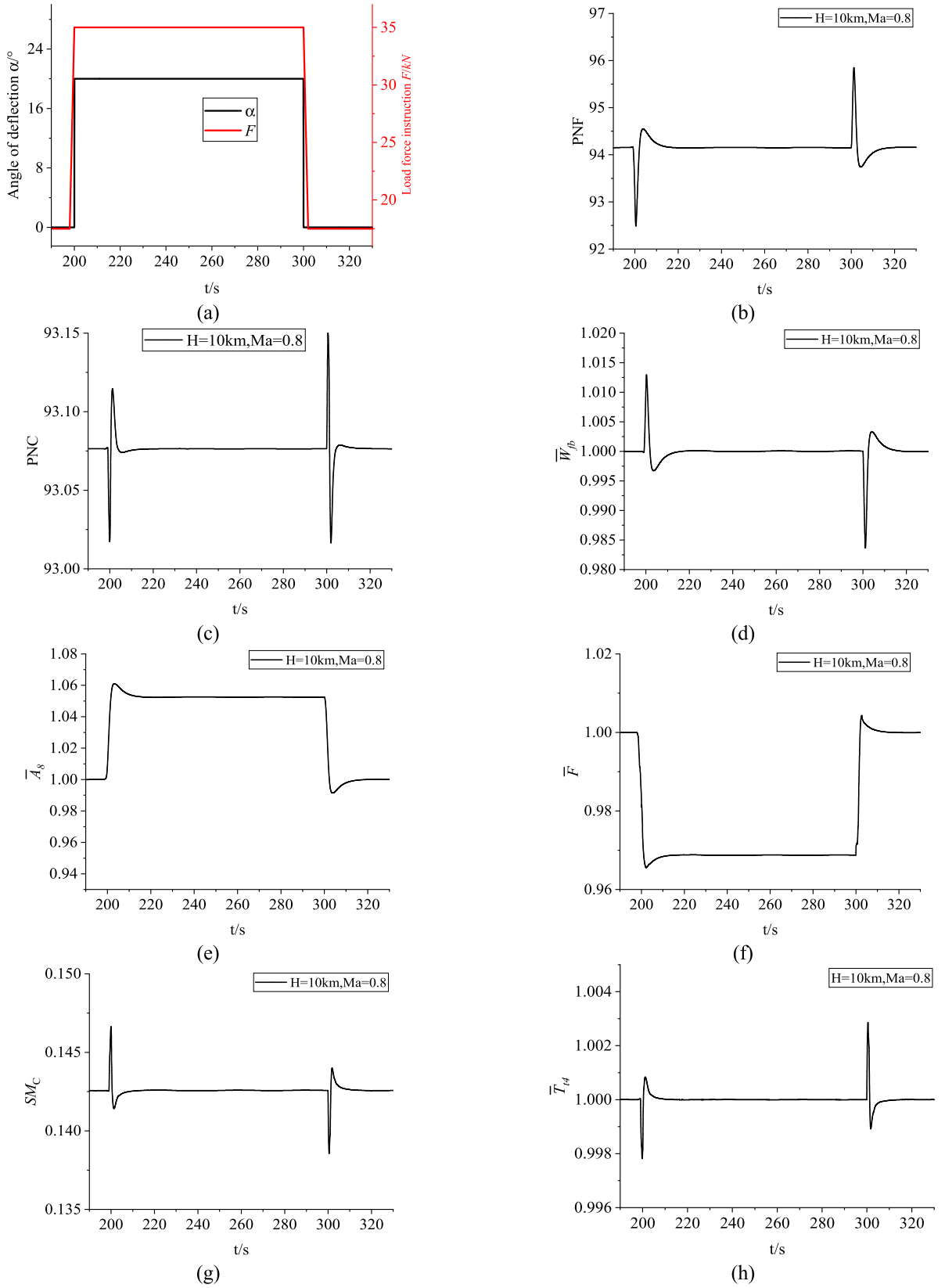

FIGURE 17. Simulation results of subsonic cruise state vector deflection.

the vector deflection angle, the more drastic the change of the load force of the A8 actuator, resulting in the greater the change amplitude of the output displacement of the actuator, and the displacement change of the A8 actuator at the high altitude point is smaller than that at the ground point.

D. INTEGRATED MODEL SIMULATION

Open-loop simulation of the established engine component-level model is carried out, and the instruction of ramp fuel supply law as shown in Figure 17 is input. The relative physical speed and thrust response of the low-pressure rotor of the engine basically meet the expected dynamic and steady-state performance of the engine.

In the high-altitude cruise state, the vector deflection signal shown in fig. 17(a) that quickly deflects 20 degrees and then returns to the center is input to the comprehensive model, and the load change instruction corresponding to the vector deflection shown in fig. 17(a) is input at the same time. The simulation results are shown in figs. 17 (b)∼(h).

From Figure 17(b)∼(f), it can be seen that the response of engine performance parameters is consistent with the theoretical calculation and aerodynamic simulation results. When the vector deflection increases, the effective throat area decreases and the engine flow decreases, which leads to the rapid decline of engine thrust and speed. Under the action of closed-loop controller, the engine fuel supply rate increases and the nozzle expands to increase the inlet flow.

As can be seen from Figure 17(g)∼(h), vector deflection has little influence on compressor rotor speed and turbine front temperature, but the response of engine speed and other parameters fluctuates greatly, with the maximum variation of fan speed of about 1.78% and high pressure surge margin of about 2.88%.

VI. CONCLUSION

In this paper, a comprehensive model of two-dimensional vector nozzle/actuator load/turbofan engine is proposed and established. The multidisciplinary coupling simulation of electromechanical integration of two-dimensional vector nozzle is realized, and the load spectra of A8 and A9 actuators during vector deflection are obtained, which makes up for the lack of understanding of the coupling characteristics between vector nozzle and engine. The main conclusions are as follows:

(1) During vector deflection, the resultant force on the upper and lower tabs of the convergent section of the two-dimensional vector nozzle remains basically unchanged, while the resultant force on the upper tab of the divergent section increases continuously, while the resultant force on the lower tab decreases slightly.

(2) With the increase of vector deflection angle, the load force on A8 and A9 actuators fluctuates greatly, among which the load force on the upper A8 actuator changes the most. When the vector deflection is 20, the load force on the upper A8 actuator increases by about 2 times, and the output displacement fluctuates by 1.225%, which affects the stable control of the vector deflection process A8.

(3) Vector deflection will change the effective throat area and thrust coefficient of the engine nozzle, which will lead to severe fluctuation of engine performance parameters. The maximum variation of fan speed is about 1.78%, and the maximum variation of high pressure surge margin is about 2.88%, but it has little effect on compressor rotor speed and turbine front temperature.

(4) Vector deflection will cause changes in the effective throat area, thrust coefficient and actuator load of the engine nozzle, which will lead to fluctuations in the output displacement of the nozzle actuator and the output fluctuation of A8 area, and then lead to unstable control of the engine. As a disturbance in engine operation, vector deflection needs to design a reasonable controller to meet the control accuracy and stability.

(5) The comprehensive model of two-dimensional vector nozzle/actuator load/turbofan engine based on mechanism is of great significance for the stability and accurate control of the engine and nozzle in engineering, and the modeling method has important reference value for establishing a multidisciplinary coupling model similar to a complex mechanism.

REFERENCES

[1] F. Capone, "The nonaxisymmetric nozzle—It is for real<149>fighter aircraft performance viewpoint," in *Proc. Aircr. Syst. Technol. Meeting*, Aug. 1979, p. 1810.

[2] Z. Cui and Y. Wang, "Summary of research on aircraft thrust vector nozzle," *Aerosp. Technol.*, vol. 12, pp. 158–167, Jan. 2021.

[3] S. Ren, J. Hong-Hu, L. Chang-Chun, H. Wei, and L. Hao-Hao, "Model experiment and numerical analysis on infrared character and infrared suppression by cooling of two-dimensional convergent-divergent nozzle," *J. Propuls. Technol.*, vol. 35, no. 4, pp. 463–469, 2014.

[4] F. Chang-De, "Developing status of thrust vectoring control technology," *Aeronaut. Sci. Technol.*, vol. 2, pp. 10–12, Mar. 1998.

[5] H. F. Wang, "Key technologies and future applications of thrust vectoring on fighter aircraft," *Acta Aeronautica et Astronautica Sinica*, vol. 41, no. 6, 2020, Art. no. 524057, doi: 10.7527/S1000-6893.2020.24057.

[6] X. Yu and Z. Xing-You, "Application of thrust vector control technology for fighter engine," *Aeroengine*, vol. 34, no. 4, pp. 56–58, 2008.

[7] B. L. Berrier and R. J. Re, "Effect of several Geometric parameters on the static internal performance of three nonaxisymmetric nozzle concepts," Tech. Rep. NASA-TP-1468. 1979.

[8] S. Syed, J. Erhart, and E. King, "Application of CFD to pitch/yaw thrust vectoring spherical convergent flap nozzles," in *Proc. 26th Joint Propuls. Conf.*, Jul. 1990, p. 2023.

[9] A. Hamed and C. Vogiatzis, "Overexpanded two-dimensional convergent-divergent nozzle performance, effects of three-dimensional flow interactions," *J. Propuls. Power*, vol. 14, no. 2, pp. 234–240, Mar. 1998.

[10] W. Wei, Z. Zhen, J. Wen-Dong, and D. Hong-Wei, "Numerical simulation of serpentine 2-D vectoring nozzle based on shock wave control," *Aeroengine*, vol. 17, no. 5, pp. 19–25, 2021.

[11] G. Xiao, Y. Qing-Zhen, L. Shu-Hao, and W. Zhen-Hua, "Research on the aerodynamic and RCS characteristics of spherical convergent flap nozzle," *Gas Turbine Exp. Res.*, vol. 34, no. 4, pp. 44–48, 2021.

[12] W. Jian-Ming, L. Si-Qi, Q. Xiao-Hang, M. Xiao-Dong, and W. Cheng-Jun, "Unsteady flow characteristics of dual-slots injection ports shock-induced thrust vectoring nozzle," *Gas Turbine Exp. Res.*, vol. 34, no. 1, pp. 5–13, 2021.

[13] A. Hadjadj, Y. Perrot, and S. Verma, "Numerical study of shock/boundary layer interaction in supersonic overexpanded nozzles," *Aerosp. Sci. Technol.*, vol. 42, pp. 158–168, Apr. 2015.

[14] G. Kang and Q. Wang, "Computational investigation on infrared radiation characteristic for two-dimensional vectoring nozzles with fluidic injection," in *Proc. Int. Conf. Transp., Mech., Electr. Eng. (TMEE)*, Dec. 2011, pp. 2174–2177.
[15] S. Zhong, D. Liu, L. Lin, M. Zhao, X. Fu, and F. Guo, "A novel anomaly detection method for gas turbines using weight agnostic neural network search," in *Proc. Pacific Int. Symp. Advanced Rel. Maintenance Model. (APARM)*, 2020, pp. 1–6.
[16] V. K. Murugesan, A. K. S. Moorthi, and G. S. L. Ramachandran, "Aspect ratio effect on Mach 1.5 rectangular jet mixing," *IEEE Access*, vol. 9, pp. 73671–73677, 2021.
[17] Z. Hai-Bo, C. Chang-Peng, and J. Shang-Bin, "Research on vector deflection loading characteristics of axisymmetric vector nozzle actuation system," *J. Nanjing Univ. Aeronaut. Astronaut.*, vol. 52, no. 4, pp. 523–531, 2020.
[18] J.-J. Huang, "Modeling and simulation of vectoring thrust nozzle control device," Nanjing Univ. Aeronaut. Astronaut., Nanjing, China, 2014.
[19] W. Yong, C. Chang-Peng, J. Wei, Z. Hai-Bo, and Z. Qian-Gang, "Thrust vector turbofan engine model and vector deflection stability control device," Tech. Rep., 2022.
[20] Q. Yu-An, X. Shou-Sheng, and S. Zhi-Ping, "Research of turbofan engine transient process with thrust vectoring nozzle," *J. Aerosp. Power*, vol. 2005, no. 1, pp. 29–32, 2005.
[21] L. Ying-Jie, W. Lin-Feng, and L. Chun-Wen, "Modeling and control of a micro aero-engine thrust vector system," *J. Tsinghua Univ.*, vol. 60, no. 3, pp. 198–205, 2020.
[22] L. Na, J. Hong-Hu, H. Wei, C. Jun, S. Ren, and L. Chang-Chun, "Comprehensive design of aerodynamic and infrared stealth of 2-D convergent nozzle with mixed flow," *J. Aerosp. Power*, vol. 26, no. 11, pp. 2563–2570, 2011, doi: 10.13224/j.cnki.jasp.2011.11.012.
[23] L. Jing and W. Qiang, "Computation for the effect of turbulence models on internal performance for axisymmetric vectoring exhaust nozzles," *J. Propuls. Technol.*, vol. 24, no. 4, pp. 326–329, 2003.
[24] D. Y. Bin, "An improved hydraulic servo predictive control system," *Mach. Tool Hydraul.*, vol. 51, no. 1, pp. 101–106, 2023.
[25] R. Bao, Q. Wang, and T. Wang, "Moedling and control strategy of a multi-pump multi-actuator hydraulic system with on/off valve matrix," *IEEE Access*, vol. 9, pp. 529–541, 2021.
[26] M. K. Liu, D. Qian, and T. Dewen, "Research on sliding mode control strategy of electro-hydraulic position servo system of valve-controlled asymmetric hydraulic cylinder," *Construct. Machinery Equip.*, vol. 54, no. 1, pp. 78–81&9, 2023.
[27] Y. Zhang, J. Shi, S. Wang, and Y. Zhang, "A multi-source information fusion fault diagnosis method for vectoring nozzle control system based on Bayesian network," in *Proc. Asia–Pacific Int. Symp. Adv. Rel. Maintenance Model. (APARM)*, Aug. 2020, pp. 1–6.

YUAN WANG received the Ph.D. degree from the Nanjing University of Aeronautics and Astronautics, in 2015. He is currently a Senior Engineer with the AECC Aero Engine Control System Institute. His research interests include modeling and the control of aero-engines.

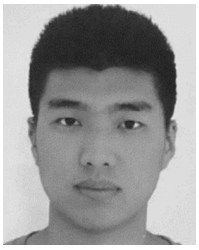

WEI JIANG received the B.Eng. degree from the Nanjing University of Aeronautics and Astronautics (NUAA), China, in 2021, where he is currently pursuing the master's degree in aerospace propulsion engineering with the College of Energy and Power Engineering. His research interests include modeling and the control of aero-engines.

HAIBO ZHANG received the Ph.D. degree from the Nanjing University of Aeronautics and Astronautics (NUAA), in 2005. He is currently a Professor with the College of Energy and Power Engineering, NUAA. His research interests include modeling, fault diagnosis, and the control of aero-engines.

QIANGANG ZHENG received the Ph.D. degree from the Nanjing University of Aeronautics and Astronautics (NUAA), in 2018. He is currently an Associate Research Fellow with the College of Energy and Power Engineering, NUAA. His research interests include modeling, fault diagnosis, optimization control, and the model predictive control of aero-engines.